

# A Whisker-inspired Fin Sensor for Multi-directional Airflow Sensing

Suhan Kim<sup>1</sup>, Regan Kubicek<sup>1</sup>, Aleix Paris<sup>2</sup>, Andrea Tagliabue<sup>2</sup>, Jonathan P. How<sup>2</sup>, and Sarah Bergbreiter<sup>1</sup>

**Abstract**—This work presents the design, fabrication, and characterization of an airflow sensor inspired by the whiskers of animals. The body of the whisker was replaced with a fin structure in order to increase the air resistance. The fin was suspended by a micro-fabricated spring system at the bottom. A permanent magnet was attached beneath the spring, and the motion of fin was captured by a readily accessible and low-cost 3D magnetic sensor located below the magnet. The sensor system was modeled in terms of the dimension parameters of fin and the spring stiffness, which were optimized to improve the performance of the sensor. The system response was then characterized using a commercial wind tunnel and the results were used for sensor calibration. The sensor was integrated into a micro aerial vehicle (MAV) and demonstrated the capability of capturing the velocity of the MAV by sensing the relative airflow during flight.

## I. INTRODUCTION

Whiskers achieve high-level interpretation on the mechanics of the whisker body by taking advantage of densely located sensory cells inside follicles [1]. When an external load is applied to a whisker, the forces and moments are transmitted through the whisker body resulting in the deformation of the follicle. This deformation is then converted to neural signals by mechanoreceptors [2]. The external load does not necessarily have to occur from contact, but it can also occur from fluid flow around the whisker. In fact, there are many examples of animals which exploit the flow sensing capability of their whiskers. Rats use whiskers not only to detect contact but to sense airflow during the whisking motion [3]. Seal whiskers are well-known for their water flow sensing ability [4]. Bats have whiskers (or hairs) located on their wings that are used to collect airflow information for feedback during flight [5]. These examples suggest that whiskers can be an efficient structure to sense airflow.

Whisker sensory systems in nature demonstrate promising features when observed from a mechatronic airflow sensor standpoint. Conventional methods such as using mechanical forces (mechanical anemometer), temperature response by heat transfer (hot wire anemometer [6]), or pressure differentials (pitot tube [7]), have focused on extracting the magnitude of the airflow velocity. However, an advantage of using a whisker structure is that it is also able to sense the direction of the airflow, which can be implemented into

This research effort was supported by Air Force Office of Scientific Research MURI award number FA9550-19-1-0386 and the National Science Foundation (NSF) award number BCS-1921251.

<sup>1</sup>Department of Mechanical Engineering, Carnegie Mellon University (CMU), Pittsburgh, PA, USA. Corresponding author: Prof. Sarah Bergbreiter (sbergbre@andrew.cmu.edu)

<sup>2</sup>Department of Aeronautics and Astronautics, Massachusetts Institute of Technology (MIT), Cambridge, MA, USA. {aleix, atagliab, jhow}@mit.edu

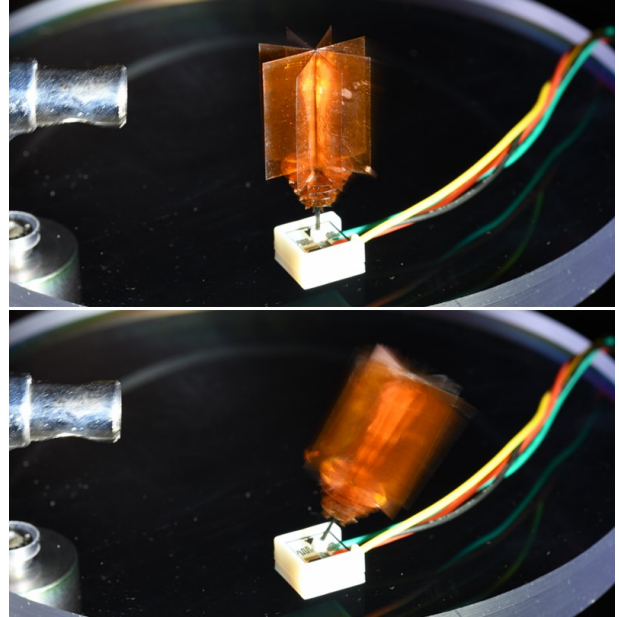


Fig. 1. Fin sensor prototype at rest (top) and under airflow (bottom).

more diverse applications. Unlike fixed wing aircraft, which have the direction of the dominant airflow predetermined, drones operate in various directions which require a multi-directional airflow sensor to track the airflow during flight.

Given this inspiration from nature and motivation from the mechatronics side, there have been many previous approaches to develop whisker structures (or similarly hair structures) for airflow sensing. A common feature is that the whisker body does not have sensing functionality, but the flow is sensed only from the information at the follicle base. Using the transduction at the base, approaches can be categorized into resistive [8], [9], contact-resistive [10], capacitive [11], optical [12], or magnetic [13] sensors. Depending on the type of transduction used, there are trade-offs between sensing range, sensitivity, durability, stability, and system integration.

However, when considering the requirements of airflow sensing, the magnetically transduced whisker which was previously introduced by the authors [13], has several aspects which make it well-suited for airflow sensing. This sensor design was capable of sensing the direction and magnitude of an external load, and also demonstrated that the sensor can capture the dynamic motion of the whisker body. Furthermore, the system utilizes a small, low-cost 3D magnetic hall effect sensor which does not require complicated circuitry thus simplifying system integration.

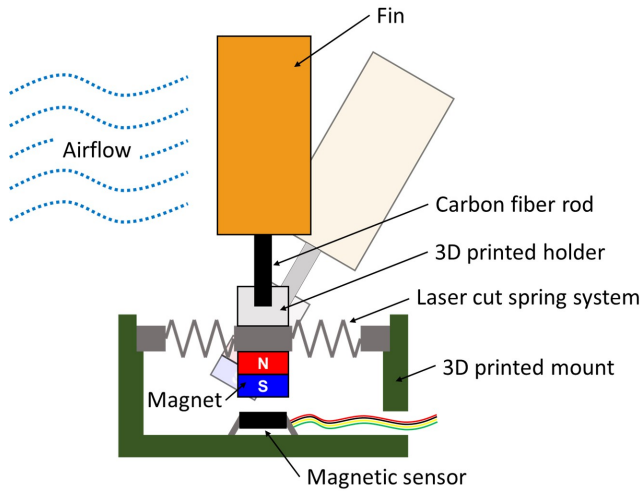


Fig. 2. Airflow sensing schematic of fin sensor. A fin and a permanent magnet are attached to the spring suspension and the magnetic field sensor is located behind.

In this work, we present the design of a 'fin sensor', an improved version of the previous whisker sensor particularly with respect to the airflow sensing functionality. Firstly, the fin structure is fabricated to obtain high air drag and multi-directional response; higher drag is required because the vast majority of transduction methods do not rival the sensitivity of whisker follicles in biology. Taking advantage of the small size of magnetic field sensor, a compact sensor module was devised which can be easily integrated into applications. In the design stage, the dimension parameters of the fin and the spring stiffness were optimized along the analytical model to improve the system performance. Then, the prototype was fabricated and characterized with a commercial wind tunnel. The collected data provided the calibration to map the magnetic sensor response to the speed and direction of the airflow.

After the analysis of the sensor functionality, the sensor was attached to a micro aerial vehicle (MAV) and data was collected during flight. By operating the MAV in a static air environment, the sensor was able to capture the velocity by measuring the relative airflow. This suggests that the presented sensor can become a simple and efficient solution for wind and airflow sensing, for a variety of applications such as simultaneous drag and interaction force estimation, and wind gust detection for flight in challenging weather conditions [14].

## II. METHODS

### A. Concept

Figure 2 shows the concept of the proposed sensor design. The sensor structure consists of a fin, spring suspension, a permanent metal magnet beneath the spring, and a magnetic hall effect sensor at the bottom. When the sensor is subjected to airflow, the fin moves along the air dragging force suspended by the spring stiffness which causes the magnet to move. The magnet motion can then be measured by the

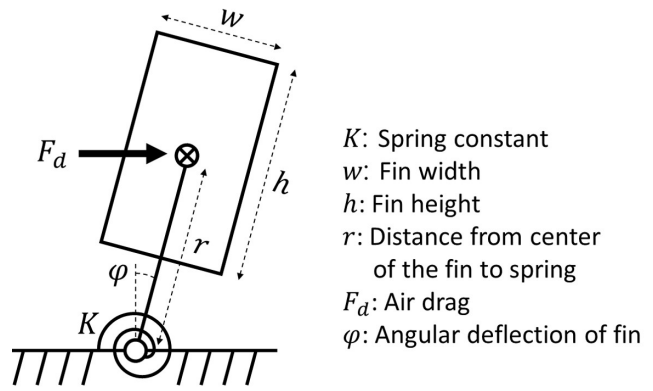


Fig. 3. Torsional spring model of the airflow sensing system with modeling parameters.

magnetic sensor. In order to increase the drag coefficient, the fin was designed to be concave toward the airflow. To achieve consistent dragging force from every direction of the flow, the fin has 8 wings with consistent  $45^\circ$  angular gap between each wing. The sensor structure was attached to a 3D printed case which is fully modularized, and was connected to the system using four wires for I2C communication. Also, the top part, composed of the fin, spring, and the magnet, and the bottom part with sensor and wires, were designed as a mechanical assembly, which brings convenience to the system integration.

### B. Modeling and design optimization

1) *Spring and magnetic model*: The sensor design uses a planar spring system that consists of four serpentine shaped springs. This type of arrangement is a well-defined mechanical suspension system. By applying Castigliano's theorem to each beam element in the springs [15], the displacement of the center square plate in the spring system can be related to the total force and torque applied to the springs. Considering the mechanism of airflow sensing of the fin sensor, vertical translation of the center square plate becomes negligible compared to rotation, since the load from vertical direction is very low. This justifies the assumption that the whisker undergoes pure rotation with the origin as the center of the spring system. With this assumption, the spring constant becomes a function of the geometric parameters of the spring as well as its material property [13].

Once the displacement of the center plate in the spring is defined, the position and rotation of the magnet can be calculated. The position of the magnetic sensor with respect to the magnet is then determined, providing the magnetic flux density at the point. The magnetic field generated in a 3D space from a cubic magnet can be described as closed form, which is a function of the property of the magnet with its position in space [16]. Finally, a rotation matrix translates the vector from magnet-centered coordinate to sensor-centered coordinate and the values of the sensor reading can be estimated analytically. More details of this approach can be found in previous work by the authors [13].

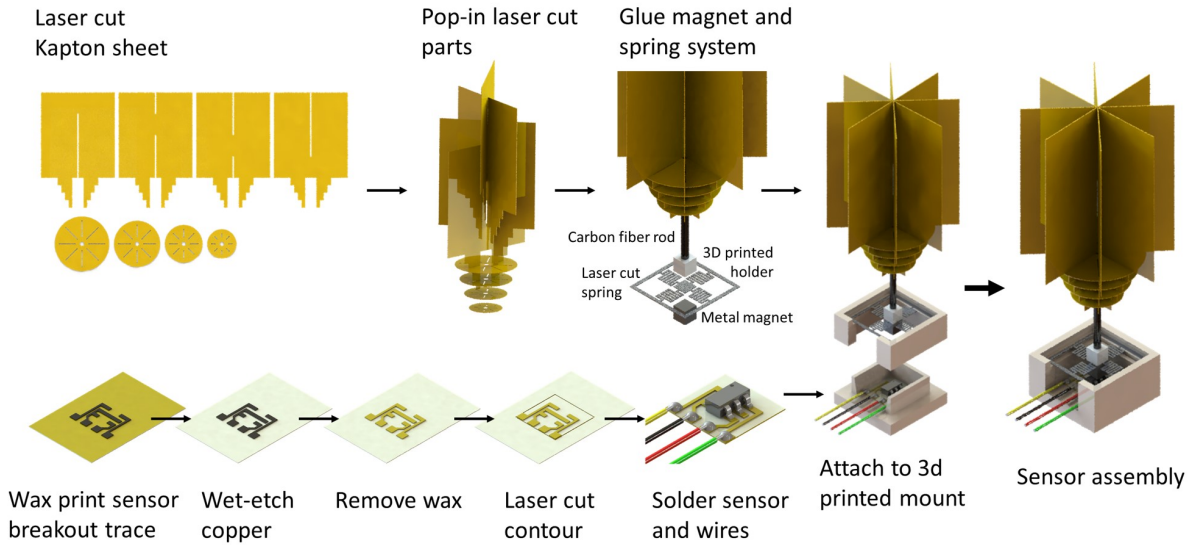


Fig. 4. Respective fabrication steps for the top part (upper stream) and bottom part (lower stream) of the fin sensor.

2) *Optimization*: During the sensor hardware iteration, an issue was raised that the inertia of the fin, when perturbed, causes oscillation of the sensor and produces an undesired signal. Effectively, the fin sensor was behaving as an inertial sensor in addition to a flow sensor. Taking advantage of multiple design parameters, an optimization was performed to minimize the oscillation of the sensor. The sensor structure was first modeled as torsional mass spring system. The settling time of the system given a step input was chosen to be the objective function for optimization, because minimizing the settling time would reduce the effects of the oscillation. The settling time of the sensor is proportional to the reciprocal of the product of damping ratio and natural frequency. However the damping could not be controlled in the proposed design, so the objective function for the negative null form was taken to be the reciprocal of the natural frequency. Selecting the objective function as described has another advantage in signal processing. As the natural frequency increases, the additional signal from oscillations would appear at a higher frequency, and could be filtered out during the signal processing step.

$$\omega_n = \sqrt{K/I} \quad (1)$$

Where  $I$  is the inertia of the fin and  $K$  is spring constant. The inertia of the fin can be calculated by summing the inertia of three separate parts.

$$I = I_{wing} + I_{support} + I_{rod} \quad (2)$$

$I_{fin}$  is the inertia of 8 wings,  $I_{support}$  is the inertia of the bottom supporting circular features, and  $I_{rod}$  is the inertia of

carbon fiber rod.

$$I_{wing} = \frac{m_{wing}}{48} \left( (h^2 + w^2) + (h^2 + t^2) + (w^2 \cos^2 \frac{\pi}{4} + t^2 \sin^2 \frac{\pi}{4} + h^2) + (w^2 \cos^2 \frac{3\pi}{4} + t^2 \sin^2 \frac{3\pi}{4} + h^2) \right) \quad (3)$$

Here,  $t$  is the thickness of fin material and  $m_{wing}$  is the mass of wings which becomes the total volume of the wings multiplied by the material density.

$$m_{wing} = 4\rho_{wing}t \cdot w \cdot h \quad (4)$$

Four parameters were chosen as the optimization variables; width of the fin, height of the fin, distance from the center of the fin to the spring, and the spring stiffness. These parameters were chosen due to ease of alteration during fabrication. The boundary for the width of the fin was qualitatively determined to prevent the wings from bending. As the fin becomes wider, wings are likely to bend due to the thinness of the material, resulting in a loss of air drag. It was observed that wings up to 10 mm width did not undergo this issue, so the boundary for total fin width was set as a maximum of 20 mm. The height of the fin and the distance from the center of the fin to the spring was upper-bounded by 50 mm respectively, which turned out to be a sufficient value to find the global minimum.

The limits for the spring constant were set along the manufacturability of the spring. Since the serpentine spring structure can be regarded as an array of beam elements, the spring becomes stiffer when the width of the beam increases. However, under given material properties (100  $\mu$ m stainless steel sheet), laser cutting the spring narrower than 100  $\mu$ m width resulted in low-quality outcomes. In these cases, the laser power is too high for the beam's aspect ratio. In addition, when the gap between the beam elements became less than 100  $\mu$ m, the fabrication also did not go well. This

is because the cut-off parts were not fully removed, leaving burnt material filling the gaps in the serpentine spring. These limitations provided the upper bound of the beam width, along with the spring stiffness.

Optimization constraints reflected the sensitivity, sensing range, and the geometry of the system. The airflow sensing range of the sensor targeted the typical velocity of a gust (10 m/s) that drones can encounter. The range of angular displacement of the fin was restricted to  $20^\circ$  of rotation in any direction, as the spring structure showed durability within this range. These aspects of the system were considered to obtain optimal sensitivity, such that the sensor would be at the deformation limit when maximum airflow is applied. This can be represented as the equation shown below.

$$\begin{aligned} K \cdot \varphi_{Max} &= F_d \cdot r \cos \varphi_{Max} & (5) \\ &= \frac{1}{2} C_d d_{Air} v_{max}^2 \cos \varphi_{Max} \cdot w \cdot h \cdot r & (6) \end{aligned}$$

where,  $\varphi_{Max}$  is the maximum angular displacement of the fin ( $20^\circ$ ),  $F_d$  is drag from the airflow,  $C_d$  is the drag coefficient of the fin,  $d_{Air}$  is volume density of air ( $1.225 \text{ kg m}^{-3}$ ), and  $v_{Max}$  is the maximum velocity in the targeted sensing range ( $10 \text{ ms}^{-1}$ ). The drag coefficient of the fin was approximated as the typical drag coefficient of a wedge structure (2.20).

The bottom feature of the fin poses the geometric constraint that the distance from the center of the fin to the spring should be 10 mm longer than half of the height of the fin. This relationship provides an inequality constraint used in optimization. Sequential quadratic programming (SQP) was used for the optimization. To avoid finding local minima, optimization was performed from multiple different starting points that can cover entire design space. Summing up all the conditions as negative null form is presented below.

$$\begin{aligned} \text{minimize}_{X=[K,w,h,r]^T} \quad & 1/\omega_n^2 = \\ & (0.0092wh(2w^2 + 4h^2 + 5.806 \times 10^{-9}) \\ & + 0.442whr^2 + 3.142 \times 10^{-4}r^3 \\ & + 3.610 \times 10^{-5}r^2 + 2.829 \times 10^{-10})/K \end{aligned}$$

$$\begin{aligned} \text{subject to} \quad & h(X) = 0.35 \cdot K - 126.62 \cdot w \cdot h \cdot r = 0 \\ & g(X) = 0.5 \cdot h - r + 0.01 \leq 0 \end{aligned}$$

$$\text{such that} \quad \begin{bmatrix} 0.00091 \\ 0 \\ 0 \\ 0 \end{bmatrix} \leq X \leq \begin{bmatrix} 0.01230 \\ 0.02 \\ 0.05 \\ 0.05 \end{bmatrix}$$

### C. Fabrication

Figure 4 depicts the fabrication of the sensor. The top and bottom part of the sensor were fabricated separately, and after the completion of each process, the two parts were assembled mechanically. Fabrication of both parts is described below.

1) *Top part:* Fabrication of fin starts by laser cutting (Photolaser U3, LPKF) a 3 mil polyimide film (Kapton Polyimide films, Dupont) into four parts with different geometry. Each part has a gap at the center with different locations, so the parts can be slid into each other. This results in a structure of eight wings attached to the center axis. In order to maintain an even angular spacing between the wings, a circular support structure was designed at the bottom. By implementing multiple layers of supporting structures, fabrication error due to the thinness of the material was minimized. Holes with 1 mm diameter were cut in all the supporting structures, and after the fin assembly, the holes served as alignment marks to attach the carbon fiber rod beneath the fin. Although polyimide film is originally a very thin and flexible material, by constructing the slide-in assembly, the center axis became rigid reducing the loss in the drag force due to the bending of wings.

The fin assembly was then glued to top of the micro-fabricated spring system using a 3d printed holder (Objet 30, Stratasys). A  $100 \mu\text{m}$  thick stainless steel sheet was laser cut (Photolaser U3, LPKF) into four planar serpentine spring structures. The recipe used low cutting power with high repetition (1.7W, 400 repetitions), which aimed to minimize heating of the steel during fabrication. A  $2 \text{ mm}^3$  cubic metal magnet (C0020, Supermagnetman) was glued to the bottom of the spring, and the entire structure was attached to a 3d printed upper casing.

2) *Bottom part:* The bottom part of the sensor consists of a magnetic sensor (TLE493D-W2B6 A0, Infineon), sensor breakout circuit, soldered wire, and the case. The breakout circuit trace was printed in wax on top of copper coated polyimide sheet (Pyralux FR9130R, Dupont) using a desktop printer (ColorQube 8580, Xerox). The sheet is then soaked in a commercial etching chemical (415-1L Ferric Chloride

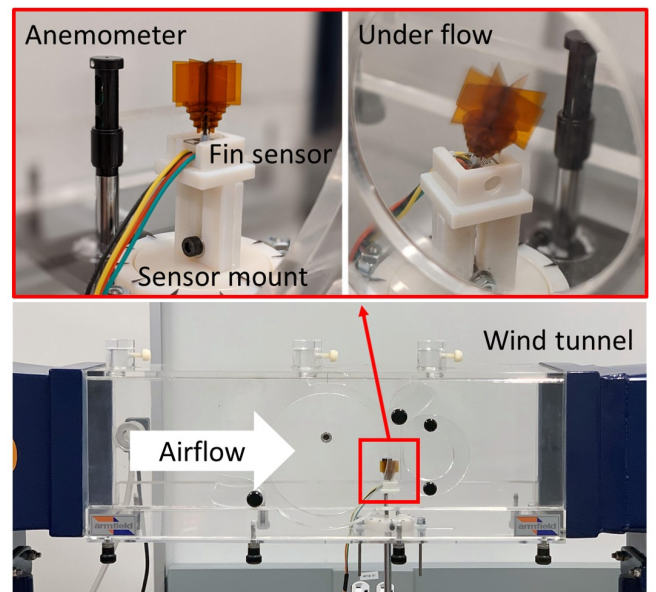


Fig. 5. Characterization setup with wind tunnel, 3d printed mount of sensor, and an anemometer.

Solution, MG Chemicals) at 45 °C for roughly 30 minutes. After etching, the copper traces with wax printed on top remains while non-covered parts are removed from the chemical reaction. Wax on the copper trace can be easily brushed off by applying isopropyl alcohol. The sheet with the circuit trace is then laser cut into 6 mm squares. The magnetic sensor and flex wires are soldered onto the PCB. The circuit was also designed such that the z-axis of the magnetic sensing inside the sensor package is located at the center of the laser cut contour (6 mm square) and aligned to the magnetization of permanent magnet after assembly. The bottom part can be completed by gluing the square sheet on the case. Since two parts of the sensor can easily be assembled and disassembled, the top part can be replaced quickly (to test a variety of fins or in case of damage) without fabricating another bottom.

#### D. Characterization

The sensor was characterized using a commercial subsonic wind tunnel (C15-10, Armfield). The wind tunnel generated airflow velocities in the desired sensing range. Although the wind tunnel was calibrated along the input of the fan to the output airflow velocity, an anemometer (4330, Thomas Scientific) was placed next to the sensor to prevent any variance of the fan performance. As shown in Figure 5, by customizing the bottom part of the wind tunnel, the fin sensor and the anemometer were able to be mounted laterally on the same position, maintaining sufficient distance so that the turbulence from one does not affect the other. A mount for the fin sensor was 3d printed which allowed the height and angle of the sensor to be adjusted using set screws. Airflow was applied from 2 m/s to 10 m/s in increments of 1 m/s. This process was repeated for 12 angular positions in 30 degree increments providing for full rotation of the sensor. Sufficient data was collected during the airflow step to catch the response from the oscillation of the sensor. Sensor data was collected using a Teensy 3.2 with a sampling rate of approximately 1 kHz.

### III. RESULTS

#### A. Design and fabrication

TABLE I

OPTIMIZED FIN DIMENSION PARAMETERS AND SPRING CONSTANT

Parameter	Value	Unit	Symbol
Spring stiffness	0.0012	$N \cdot m/rad$	$K$
Width of spring beam element	115	$\mu m$	
Width of fin	19.1	mm	$w$
Height of fin	11.3	mm	$h$
Distance from center of fin to spring	21.6	mm	$r$

Resultant values from the optimization are shown in Table I. A prototype was fabricated from the optimized parameters as in Figure 6(a). From the optimized value of spring constant, the width of the beam element was calculated to be 115  $\mu m$  and the fabrication of the spring resulted in acceptable precision. Total size of the spring was 10 mm

square and the mount for the sensor became 12 mm square for its bottom surface area.

#### B. Sensor characterization

Figure 7 presents the magnetic field response with respect to the airflow in x and y directions, where the directions are the sensing directions of the magnetic sensor. Negative airflow is the flow from the reversed direction, which was obtained by rotating the sensor 180 degrees in the wind tunnel. Error bars came from the standard deviation of the data acquired in a certain amount of time, and this represents the oscillation at a given flow speed. The magnetic field response was well-decoupled along the direction of the airflow, and demonstrated a one-on-one relation to the airflow for the entire sensing range. This suggests that the flow speed can be estimated from sensor data. A higher velocity in airflow resulted in larger oscillations, and the error bars increased accordingly. Although the noise (or error) of the sensor was higher for the faster airflow range, the slope of the response became larger which compensates for and maintains the resolution of the system. A maximum of 10 m/s airflow resulted in 50 mT of magnetic field change.

The airflow directed between the x and y axes prompted a response both in  $B_x$  and  $B_y$ . Figure 8 plots the response for 12 different directions (every 30 degrees of rotation) when maximum airflow is applied. The magnitude of the change in  $B_x$  and  $B_y$  responded to the direction of the flow, drawing sinusoidal relations as expected.

#### C. System calibration

The magnitude of the magnetic field response is a one-to-one map with the speed of airflow in a given direction. The direction is related to the ratio of the response in  $B_x$  and  $B_y$ . These relationships allow the system to be calibrated for the speed and direction of the airflow. The experiment resulted in 10 data points for 12 different directions. The system calibration was performed using these 120 data points. The speed of the airflow was mapped to the norm of the vector  $[B_x, B_y]$  which showed agreeable consistency among 12 different directions. The relation was approximated to a quadratic function with  $R^2 = 0.955$ . The direction of the

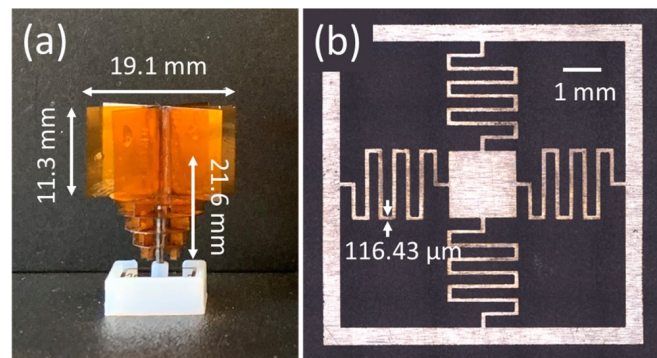


Fig. 6. (a) Prototype of optimized fin sensor with dimensions. (b) Microscope (LSM800, Zeiss) picture of the spring with fabrication result values and scale bar.

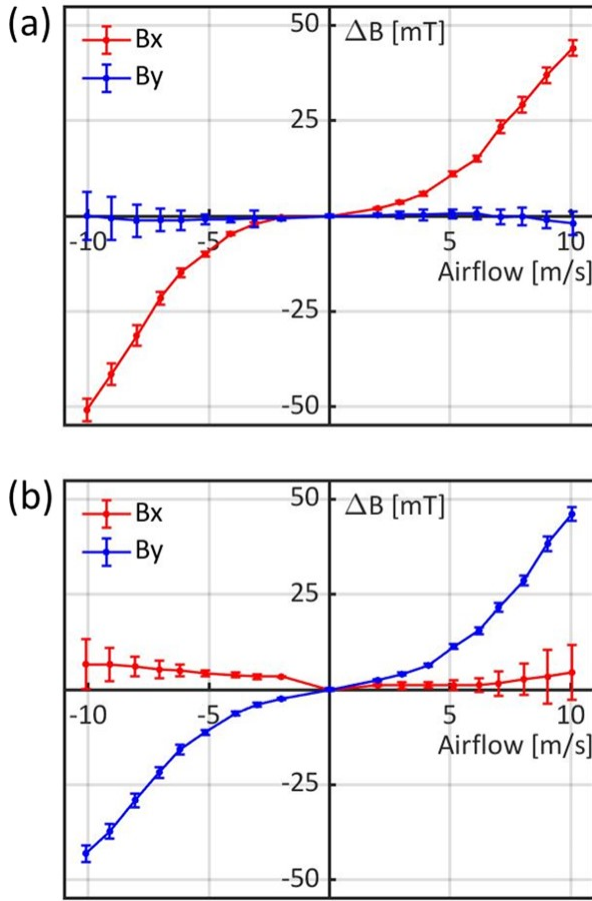


Fig. 7. Magnetic field response when airflow is applied from (a) x direction and (b) y direction respectively.

airflow can then be estimated from the inverse tangent of the ratio between  $B_x$  and  $B_y$ , which could be calibrated by a linear equation. This gives the system calibration as follows.

**Speed** (units: m/s, mT)

$$v = -0.0033 \cdot \Delta B_{xy}^2 + 0.3361 \cdot \Delta B_{xy} + 1.2561$$

$$\Delta B_{xy} = \sqrt{\Delta B_x^2 + \Delta B_y^2}$$

$$R^2 = 0.9554$$

**Direction** (units: degree)

$$\theta = 1.0706 \cdot \arctan(B_y/B_x) - 15.866$$

$$R^2 = 0.9805$$

#### IV. APPLICATION

As MAVs become more prominent both in research and industry, the ability to fly in windy environments becomes essential [14], [17]. Therefore, in this section we demonstrate our sensor's capacity to estimate the relative airflow acting on an MAV. More details about using the proposed sensor for onboard estimation of wind, drag and other interaction

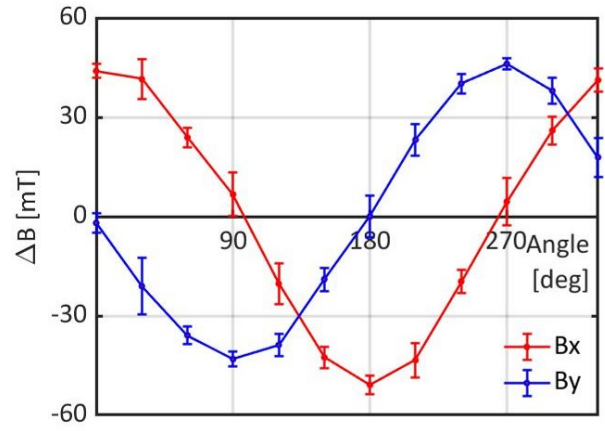


Fig. 8. Magnetic field response with respect to the direction of the airflow, when the maximum airflow is applied.

forces on an MAV can be found in our related work [18].

#### A. Test setup

The experiment aimed to estimate the velocity of the MAV by measuring the relative airflow using the fin sensor during indoor operation. The sensor was placed where the gust from propellers would not result in significant impact. A custom-made hexarotor was used with an on-board computer (Jetson TX2, Nvidia), which was able to directly interface with the sensor without a separate microcontroller. The MAV communicates through Wi-Fi, transferring the data from fin sensor and equipped inertial sensor in real time. A Vicon system was used as the ground truth testbed utilizing 24 cameras and motion trackers on the MAV which could track 6-DOFs (translation and rotation). By compiling the data from the inertial sensor on the drone and position/rotation from the Vicon system, translational and angular velocity of the MAV could be calculated. Flight control of the MAV was done using a commercial gaming controller and was operated to cover a wide range of velocities.

For the application, a new sensor design with a more robust structure was utilized. Since the spring is the most fragile structure of the sensor (due to its high aspect ratio), an additional optimized sensor was built with a relatively thicker spring width. This aimed to reduce the chance of spring damage from unexpected drone motion, gusts, or collisions. Dimensions for this prototype are presented in figure 11.

#### B. Test result

Figure 10 presents the data collected during the MAV operation. The motion of the MAV was designed to produce a diverse velocity range of up to 4 m/s, and also to obtain complex combination of x and y directional movement. The sensor demonstrated decent capability of tracking the velocity of MAV in both x and y directions with the raw data of  $B_x$  and  $B_y$ . Figure 10 (c) compares the velocity of the MAV recorded from the Vicon system with the estimation from fin sensor data. While estimation from fin sensor was able to track the velocity of MAV for the most part, mismatch

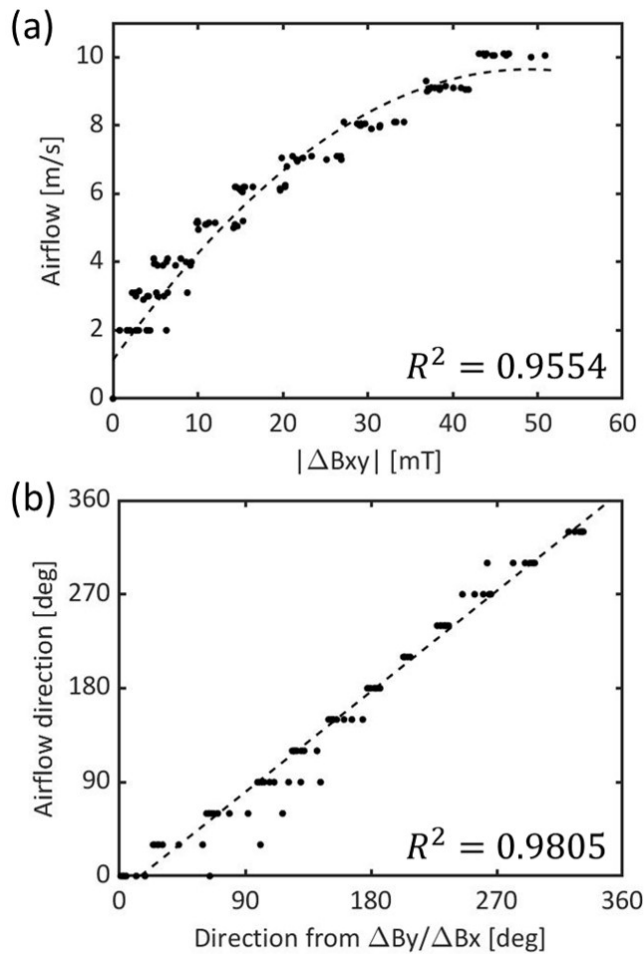


Fig. 9. Entire map of the magnetic field response to the (a) the speed and (b) the direction of the airflow with system calibration curve.

was observed particularly when MAV was moving toward y direction. It is suspected that the error appeared from characteristic curve extracted in calibration step, and this can be further improved by designing more complex filters or implementing more sensors to MAV. The data demonstrates the future application of the fin sensor as compensating for drift in inertial sensors, or for gust sensing during flight.

## V. CONCLUSIONS

This work presented an airflow sensor design inspired by whiskers in animals which is capable of sensing the speed and direction of the airflow. The sensor design consists of a fin structure suspended by a planar serpentine spring, and utilizes magnetic transduction with a small magnet beneath the spring and a magnetic sensor at the bottom. Functionality of the sensor was modeled along with the dimensions of the fin and the stiffness of the spring. Optimization was conducted with respect the dimensions to establish a design with the best performance. The sensor was characterized by applying a known airflow to the sensor and measuring the corresponding magnetic fields. The sensor was calibrated to provide the speed and the direction of the airflow from the magnetic field sensor values.

Utilizing the robust characterization and calibration of the sensor, the sensor was integrated onboard a micro aerial vehicle and tested. The sensor was able to successfully capture the velocity of the drone in the x and y directions by sensing the multi-directional speed of the relative airflow. This suggests a future use for the sensor toward correcting for the inherent drift in inertial sensors. Furthermore, it is hoped that the sensor will be able to detect a wind gust during the drone operation, which can contribute to reinforcing the controls in turbulent situations. Ultimately, future work can continue to improve these sensors further by shrinking size and enhancing robustness.

## ACKNOWLEDGMENT

This research effort was supported by Air Force Office of Scientific Research MURI award number FA9550-19-1-0386 and the National Science Foundation (NSF) award number BCS-1921251. The authors would also like to thank Prof. Yoed Rabin and Prof. Satbir Singh for the instruction and guidance in use of the wind tunnel characterization facility, and David Ma for photography.

## REFERENCES

- [1] R. A. Grant, S. Haidarliu, N. J. Kennerley, and T. J. Prescott, "The evolution of active vibrissal sensing in mammals: evidence from vibrissal musculature and function in the marsupial opossum *monodelphis domestica*," *Journal of Experimental Biology*, vol. 216, no. 18, pp. 3483–3494, 2013.
- [2] M. Szwed, K. Bagdasarian, B. Blumenfeld, O. Barak, D. Derdikman, and E. Ahissar, "Responses of trigeminal ganglion neurons to the radial distance of contact during active vibrissal touch," *Journal of Neurophysiology*, 2006.
- [3] S. Yan, M. M. Graff, and M. J. Hartmann, "Mechanical responses of rat vibrissae to airflow," *Journal of Experimental Biology*, vol. 219, no. 7, pp. 937–948, 2016.
- [4] G. Dehnhardt, B. Mauck, and H. Bleckmann, "Seal whiskers detect water movements," *Nature*, vol. 394, no. 6690, pp. 235–236, 1998.
- [5] S. Sterbing-D'Angelo, M. Chadha, C. Chiu, B. Falk, W. Xian, J. Barcelo, J. M. Zook, and C. F. Moss, "Bat wing sensors support flight control," *Proceedings of the National Academy of Sciences*, vol. 108, no. 27, pp. 11 291–11 296, 2011.
- [6] C. G. Lomas, *Fundamentals of hot wire anemometry*. Cambridge University Press, 2011.
- [7] R. Klopfenstein Jr, "Air velocity and flow measurement using a pitot tube," *ISA transactions*, vol. 37, no. 4, pp. 257–263, 1998.
- [8] Y. Ozaki, T. Ohyama, T. Yasuda, and I. Shimoyama, "An air flow sensor modeled on wind receptor hairs of insects," in *Proceedings IEEE Thirteenth Annual International Conference on Micro Electro Mechanical Systems (Cat. No. 00CH36308)*. IEEE, 2000, pp. 531–536.
- [9] H.-S. Shin, T. Kim, S. Bergbreiter, and Y.-L. Park, "Biomimetic soft airflow sensor with printed ionogel conductor," in *2019 2nd IEEE International Conference on Soft Robotics (RoboSoft)*. IEEE, 2019, pp. 611–616.
- [10] A. E.-T. Yang, M. J. Hartmann, and S. Bergbreiter, "Contact-resistive sensing of touch and airflow using a rat whisker," in *2018 7th IEEE International Conference on Biomedical Robotics and Biomechanics (Biorob)*. IEEE, 2018, pp. 1187–1192.
- [11] A. Dagamseh, C. Bruinink, H. Droogendijk, R. J. Wiegerink, T. S. Lammerink, and G. J. Krijnen, "Engineering of biomimetic hair-flow sensor arrays dedicated to high-resolution flow field measurements," in *SENSORS, 2010 IEEE*. IEEE, 2010, pp. 2251–2254.
- [12] A. Dagamseh, T. S. Lammerink, R. Sanders, R. J. Wiegerink, and G. J. Krijnen, "Towards high-resolution flow cameras made of artificial hair flow-sensors for flow pattern recognition," in *2011 IEEE 24th International Conference on Micro Electro Mechanical Systems*. IEEE, 2011, pp. 648–651.

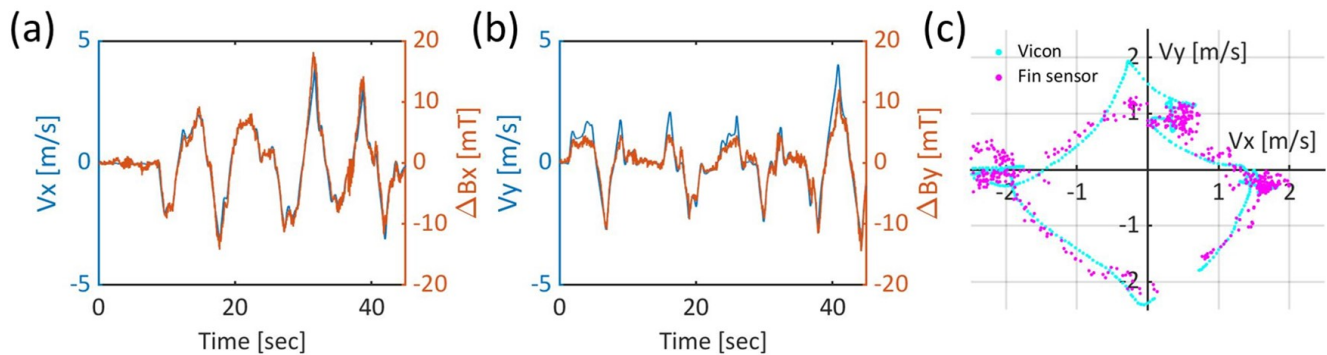


Fig. 10. Result of MAV implementation test. Time domain velocity profile with magnetic field change in (a) x-axis, and (b) y-axis. (c) Comparison between estimated velocity of MAV from fin sensor and Vicon system.

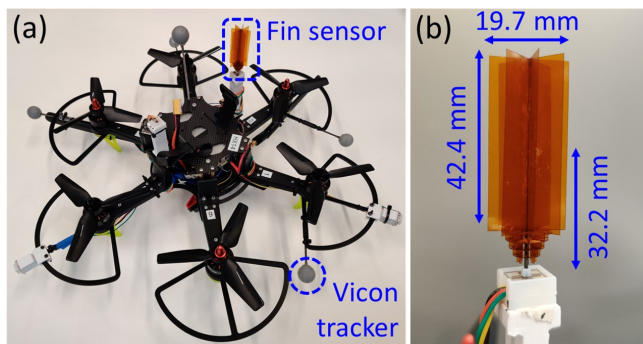


Fig. 11. MAV with fin sensor for application. (a) Picture of custom-made MAV with on-board computer, Vicon tracker, and fin sensor mounted. (b) Zoomed-up image of robustly optimized sensor with dimension parameters.

- [13] S. Kim and C. Velez, "A magnetically transduced whisker for angular displacement and moment sensing," in *IEEE/RSJ International Conference on Robots and Systems*, 2019.
- [14] A. Paris, B. T. Lopez, and J. P. How, "Dynamic landing of an autonomous quadrotor on a moving platform in turbulent wind conditions," in *2020 International Conference on Robotics and Automation (ICRA)*. IEEE, 2020, pp. 9577–9583.
- [15] H.-M. Chou, M.-J. Lin, and R. Chen, "Fabrication and analysis of awl-shaped serpentine microsprings for large out-of-plane displacement," *Journal of Micromechanics and Microengineering*, vol. 25, no. 9, p. 095018, 2015.
- [16] E. P. Furlani, *Permanent magnet and electromechanical devices: materials, analysis, and applications*. Academic press, 2001.
- [17] J. Ware and N. Roy, "An analysis of wind field estimation and exploitation for quadrotor flight in the urban canopy layer," in *2016 IEEE International Conference on Robotics and Automation (ICRA)*. IEEE, 2016, pp. 1507–1514.
- [18] A. Tagliabue, A. Paris, S. Kim, R. Kubicek, S. Bergbreiter, and J. P. How, "Touch the wind: Simultaneous airflow, drag and interaction sensing on a multirotor," *arXiv preprint arXiv:2003.02305*, 2020.